Non-Mydriatic Fundus Images Enhancement Based on Conformal Mapping Extension

Songlin Yan [1], Xiujiao Chen[2,*], Jiehua Sun[1,*], Xiaoying Tang[3], Xuebing Chi[4]

[1]Guilin Tourism University, Guilin 541006, China
[2]The Second Affiliated Hospital of Guilin Medical University, Guilin 541199, China
[3]Southern University of Science and Technology, Shenzhen 518055, China
[4]Computer Network Information Center, Beijing 100190, China
yansl@sccas.cn, (Corresponding Author: chenxiujiao@glmc.edu.cn, sunjiehua428@163.com),
tangxy@sustc.edu.cn, chi@sccas.cn

Abstract: Image enhancement is an important technique for improving observation, especially for non-mydriatic fundus images. Hence a new non-mydriatic fundus images enhancement pipeline is proposed here. Our fundamental procedure is from automatically generating the mask of the field of view (FOV) to restoring their original color. Briefly speaking, by extending the FOV region with conformal mapping, we can solve the boundary problems of image enhancement. And inspired by high dynamic range imaging (HDRI) theory, a new color restoration tactic is developed to correct the color deformation of enhanced images. To demonstrate the robustness of our algorithms, a hybrid test dataset is introduced. It not only contains some public datasets, e.g. DRIVE, Kaggle and Web (some unannotated images from a web), but also includes many private non-mydriatic datasets that were collected from the third affiliated hospital of our collaborative university. The masks were validated on DRIVE dataset by using 5 famous criteria. And we performed all enhanced results with 10 different objective image quality assessment (IQA) models. The experimental outputs of mask segmentation achieve the similarity coefficients: Cosine 99.594%, Sorensen-Dice 99.593%, Jaccard 99.19% and Pearson 98.714%, and Tanimoto 98.891%, respectively. The enhanced results from the IQA models are: BRISQE 38.9, BLIINDS2 49.87, BIQI 16.49, ILNIQE 43.39, NIQE 6.62, IFC 1.517, MS-SSIM 0.712, PSNR 21.33, SSIM 0.775, and VIF 0.2, respectively. Besides, we will opensource all programs and test codes on GitHub.

Keywords: Image enhancement; Region extension; Non-mydriatic fundus image

1 Introduction

Usually, ophthalmic patients will experience a series of painful torture when they receive dilated retinal imaging in the hospital. This is because they need to take glaucoma preclusion and then drip some compound tropicamide to dilate the pupil of the eye. After that, they have to undergo a critical step called dilated fundus examination (DFE) to detect pathological changes [1]. This complex process also results in the difficulty of obtaining fundus images. Thanks to the advance of technology, a kind of contact-free digital non-mydriatic fundus camera is being started promoting [2]. Its presence could solve the aforementioned issues. More importantly, doctors or even chronic patients can manipulate this type of camera conveniently [3].

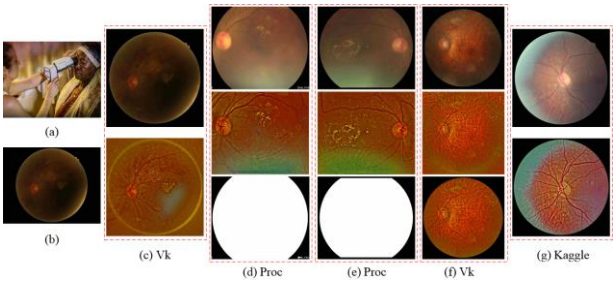

Figure 1. Demonstrations of non-mydriatic fundus imaging, different series of images and their enhanced outputs. A scene of non-mydriatic fundus imaging is shown in (a). And (b) is a sample of type "Extremely dark foreground", as mentioned in **section 2.1**. The figures (c) - (g) show different outputs of various data series, including extended results, final outputs and their masks. It should be noted that the masks of (d) and (e) are the samples of type "Direct generation" and "After fitting" respectively, which are depicted in **section 3.1**.

However, most of such cameras are used in non-medical environment as shown in Figure 1(a) [4]. In other words, their images could suffer from visual quality degradation as illustrated in Figure 1(b). To rectify image distortions, some image enhancement techniques such as Speeded Up Adaptive Contrast Enhancement (SUACE) [5] and Bandelets [6] were exploited. Besides, there are also dozens of enhancement algorithms to refine fundus images. An option to retinal image enhancement is the contrast-limited adaptive histogram equalization (CLAHE) [7]. This choice is quite reasonable for either gray scale [8, 9] or color image enhancement [10], due to its simplicity. An alternative way is the Retinex family, i.e. Single-Scale Retinex (SSR) [11] or Multi Scale Retinex (MSR) [12]. For instance, Hani et al. [13] pointed out that their enhancement technique (RETICA) could derive normalized contrast (in particular for the enhanced vessels) from linking Retinex with Independent Component Analysis (ICA). Although these algorithms have provided many great innovations for image enhancement, it is still a challenge to apply them

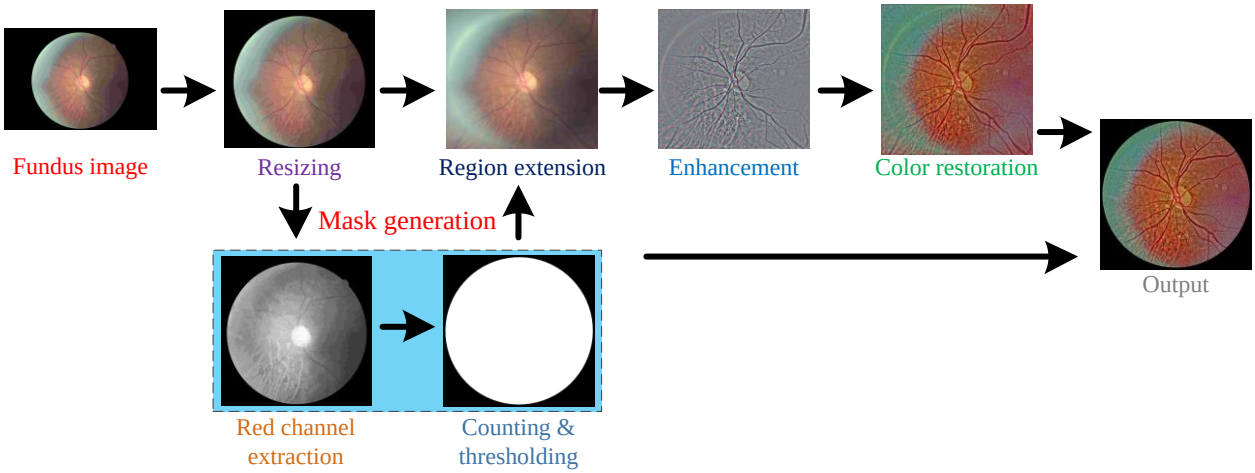

Figure 2. The flowchart of our pipeline. There are 4 key stages in our pipeline: Mask generation; Region extension; Enhancement and Color restoration.

to fundus images directly. Thus, with a large number of accessible non-mydriatic fundus images, how to improve the quality of fundus images is a tricky problem currently.

In some literatures [9], a common strategy based on gray scale image was proposed to enhance the contrast of fundus images. However, if doctors only use these colorless images, they may neglect some key pathology lesions. In addition, there are some flexible parameters in those methods. We propose a revolutionary new pipeline to enhance the artifact and poor exposed color fundus images.

Overall, our pipeline is a fixed-parameter, hands-off algorithm tree to dispose of uneven illumination and contrast variation. Its workflow builds upon the following stages: mask generation, the FOV region extension, image enhancement and color restoration. The entire idea is that, after expanding the boundary with conformal mapping, we managed heterogeneous images by simulating automatic dodging-and-burning tricks and rescuing their color successively.

Our contributions are as follows:

(1) An original extension algorithm of the FOV region is investigated by utilizing conformal mapping theory.

(2) We explicate our color revivification mechanism which restores the color of images using some specific functions in HSV (hue, saturation, value) color space.

Moreover, we tested our innovative thread on our hybrid dataset, including DRIVE [14], Kaggle [15], Web [16] and our private sub-datasets. Our test scores show that our pipeline performs excellently on both mydriatic and non-mydriatic fundus images.

2 Overview of the method and datasets

Specifically, our flowchart is demonstrated in Figure 2. An image entering this pipeline is first resized to a proper scale according to its original size. This step is not necessary, while it could reduce the computational complexity. And the composition of our datasets is listed in Table I.

Table I The overview of our datasets

	Masking statistical set	Enhancement test set	Mask benchmark set
Kaggle	4188	10	-
DRIVE	-	40	40
Web	-	6	-
Od*	-	4	-
Proc*	-	14	-
Vk*	3107	56	-
Total	7295	130	40

Please note that we use the whole Kaggle sample dataset as a part of enhancement testing set. * denotes the private dataset.

Algorithm 1: Mask generation

Require: fundus image $I(M, N,3)$, apriori information
- **Initialize:** the red channel of each image $I_r(M, N)$; the histogram of red channel $H_r(t)$;Max_0 <- 0 ; Min_e <- 255; Min_o <- 255

1. **for** k in range [31: 255] **do** Max_0 <- $max(H(k))$ **end for**
2. **if** $H(30)$ >= Max_0 **then**
   Type = *extremely dark foreground*
   for k in range [1: 21] **do** Min_e <- $min(H(k))$ **end for** T <- Min_e
   else
   Type = *others*
   for k in range [5: 21] **do** Min_o <- $min(H(k))$ **end for** T <- Min_e
   end if
3. **for** every pixel $I_r(i, j)$ in $I_r(M, N)$ **do**
   if $I_r(x, y)$ >= T **then**
   $I_r(x, y)$ = 255
   else $I_r(x, y)$ = 0
   end if
   end for
4. $I_{um}(M, N)$ <- *optimize the mask* $I_r(M, N)$; $I_m(M, N)$ <- *apply ellipse-fitting* $I_{um}(M, N)$

- **Return:** unfitted mask $I_{um}(M, N)$, ellipse-fitted mask $I_m(M, N)$

As the aforementioned, our pipeline relies on four stages. (1) *The mask generation stage*, we extract the mask from the **Red band** of each image. Here we use a priori knowledge to recognize the foreground (the FOV region). The knowledge is that the foreground is dominated by one color – Red [17]. (2) *The FOV region extension stage*, the FOV region is expanded 20 pixels in each direction by default. By developing and discarding mirroring operations, we prefer the conformal mapping extension whose pattern is more elegant in mathematics. A reasonable answer is that the relationship between the outer points (the extension part) and the inner points (the

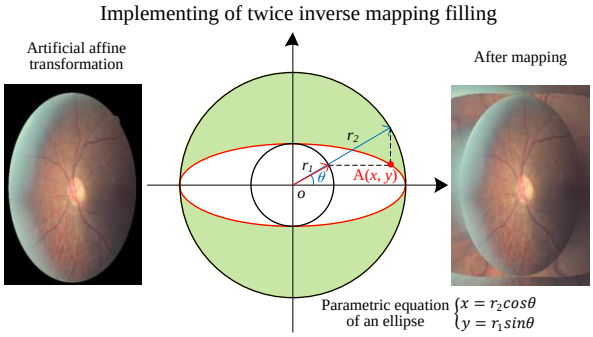

Figure 3. The application of inversion in an ellipse. The coordinates of an ellipse can be calculated by the radii of its maximum inscribed circle and minimum circumscribed circle.

FOV part) is bijection [18, 19]. More importantly, there is an insurmountable obstacle of mirroring operations when the extended distant exceeds the major axis semi-diameter of the FOV, whereas the conformal mapping extension is infinite in theory [20]. (3) *The image enhancement stage*, the combination of classic spatial models (i.e., LoG and USM) and the modified ACE algorithm can help us to enhance the textures and control the uneven luminosity. (4) *The color restoration stage*, we will restore the color of enhanced images under a series of color space conversions and color restoration functions. In the following sub-sections, we will start describing every stage in detail.

2.1 Mask generation

The masking is a convenient method to locate a region of interest (ROI), e.g. the FOV of a fundus image. Based on the red channel apriority, we first extracted the red bands from "Masking statistical set" and then collected their histograms. After preparing these materials, we conducted the statistics of these histogram data and found that there were only two types of fundus images: "Extremely dark foreground" and "Others", as shown in Figure 1(b). The details can be concluded as Algorithm 1.

2.2 FOV region extension

The FOV region is the valid region of a retinal image, and it is also known as the foreground in some cases. Naturally, the rest black part is defined as background. The drawback is that some common operations, such as filtering, convolution and fast Fourier transformation (FFT), could be influenced by the internal edges in consequence of their symmetric structured elements. Especially because of the Gibbs phenomenon [21], these symmetric elements could even bring about some severe ringing artifacts if there is a sharp edge within an image.

After extracting the masks, we could expand the FOV region to cover the background region by using conformal mapping theory. Our extension model is based on the polar coordinate system. And we suppose that there exist a point $O(r_0, \theta_0)$ out a circle C, and a point $I(r_i, \theta_i)$ in C,

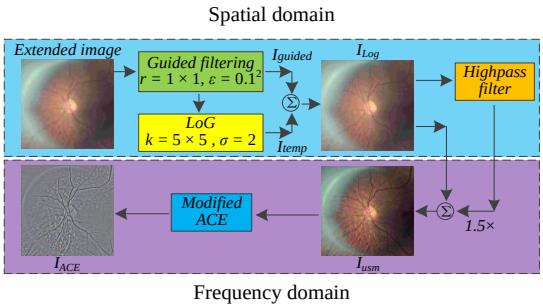

Figure 4. The overview of our enhancement framework. All of parameters in this stage are static.

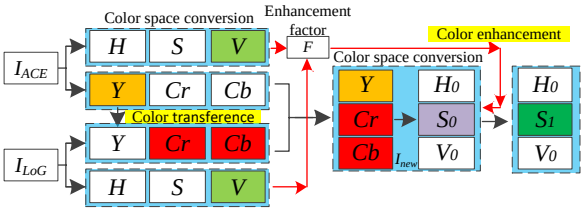

Figure 5. The framework of our color restoration method. It contains two core parts: Color transference and Color enhancement. The output will go back to RGB format after color enhancement.

$$r_0 = R^2 / r_i, \tag{1}$$

$$\theta_0 = \theta_i, \tag{2}$$

where R is the radius of C. More specific details about this process are displayed in Figure 3.

2.3 Image enhancement

As shown in Figure 4, our route can be summarized as the cooperation between spatial domain models and frequency domain algorithm. Now we comb the details and give some explanations of them.

Spatial domain models: (1) The discrete Laplacian operator is an edge sharpening technique, and it is also our first enhancement step. In order to pay tribute to this classic, we defined this method as:

$$I_{LoG} = I_{guided} + I_{temp}, \tag{3}$$

$$I_{highpass} = I_{LoG} - \tilde{I}_{guided}, \tag{4}$$

$$I_{usm} = I_{LoG} + 1.5 \cdot I_{highpass}, \tag{5}$$

where I_{guided} represents the slightly self-guided-filtered input; I_{temp} denotes I_{guided} processed by the LoG operator, I_{LoG} is the result of equation (3); $I_{high-pass}$ denotes the unsharp mask and $\tilde{I}_{guided}$ means a self-guided-filtered version ($r = 30 \times 30$, $\varepsilon = 0.1^2$) of I_{LoG} . And the normalization is a supplement to each model above.

Frequency domain algorithm: As the aforementioned, the heart of ACE model lies at color retention. Briefly speaking, when we set a set of fixed parameters: $\alpha = 8.0$, $\omega = 15$, $poly = 7$, the results show a wonderful light

distribution rather than a sharp enhancement. Please note that all parameters in our pipeline are static.

2.4 Color restoration

On account of color deformation, we explore a new methodology for color restoration as illustrated in Figure 5. At first, we convert the color spaces of I_{ACE} and I_{LoG} from RGB to YCrCb, and then replace Y_{LoG} with Y_{ACE} to generate a new image I_{new}. This process is what we call "Color transference". And we could retrieve the original hue and maintain the enhanced details. As everyone knows, a Y channel can be represented as

$$Y = 0.299 \cdot R + 0.587 \cdot G + 0.114 \cdot B. \quad (6)$$

And using Y channel to convert color image to gray-scale image is a popular manner. Thus we believe the Y channel is the best choice as the unchangeable item. However, comparing with the original, the color of I_{new} is rather light. Consequently, we have to revivify its color by color space conversion and color enhancement. Owing to the independence of HSV channels, we transform I_{ACE}, I_{LoG} and I_{new} from RGB to HSV. This transformation also ensures our computation under the same coordinate system – cylindrical coordinate system. Our strategy is that the value of each pixel in the H-V plane is constant during the enhancement. Thus we only pay attention to the value of each pixel in the S axis.

Given two points $P_0(S_0)$ and $P_1(S_1)$, we depict our enhancement by introducing a saturation channel enhancement function

$$S_1 = min\{F \cdot S_0, 1\}, \quad (7)$$

where F is the color enhancement factor, $S_0 \in [0,1]$, $S_1 \in [0,1]$, P_0 is the point before enhancement and P_1 denotes the point after enhancement. We find the enhancement factor F as follows

$$\gamma = -\log(\frac{e}{2}) / \log(\frac{1}{2}), \quad (8)$$

$$\zeta = max\{1, 1.5 \cdot V_{ACE}^{\gamma} / V_{LoG}\}. \quad (9)$$

Plugging into the saturation equation

$$Sat(x) = min\{5 \cdot \tanh\frac{x}{2}, x\}, \quad (10)$$

we get

$$F = Sat(\zeta), \quad (11)$$

where $V_{ACE} \in [0,1]$ and $V_{LoG} \in [0,1]$ denote the V channels of I_{ACE} and I_{LoG} respectively. It should be noted that all variables are computed by pixel.

(a) Cropping-Adding (C.A.) (b) Masked

Figure 6. Samples for explaining FR references. (a) is a sample of **Cropping- Adding (C.A.)** and (b) is **Masked**.

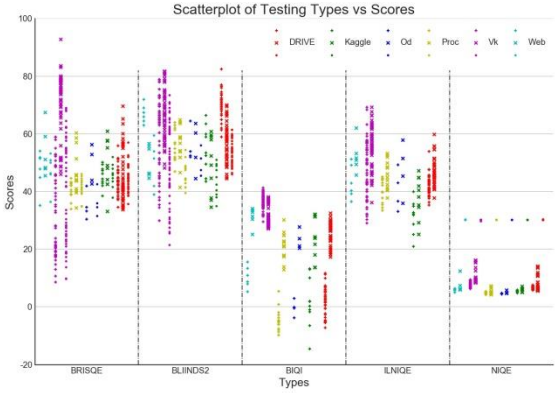

Figure 7. The overview of test results in NR family. We scrutinized all kinds of data series and scoring modes by different NR models. + denotes the result of "Y channel"; × represents the output of "Mean"; and • means the score of "Direct".

Table II Masking statistical scores based on diverse criteria

	Direct generation		After fitting	
	Avg	StDev	Avg	StDev
Cosine	0.99594	0.00102	0.97939	0.00232
Sorensen-Dice	0.99593	0.00102	0.97917	0.00236
Jaccard	0.99190	0.00203	0.95920	0.00454
Pearson	0.98714	0.00324	0.93810	0.00703
Tanimoto	0.98891	0.00279	0.94540	0.00613

Note that the table shows the scores of both types.

Table III The statistical characteristics of the whole test dataset across all NR models

	Y channel		Mean		Direct	
	Avg	StDev	Avg	StDev	Avg	StDev
BRISQE	38.90	11.44	56.79	15.06	42.12	12.45
BLIINDS2	62.35	11.05	59.91	9.82	49.87	10.06
BIQI	16.49	17.97	27.65	5.41	-	-
ILNIQE	43.39	8.50	50.09	8.30	-	-
NIQE	6.62	1.15	8.03	2.58	30.23	0.05

Please note that the smaller the value is, the better the model works.

Table IV The average scores of various FR algorithms across all the 6 data categories

	Y channel		Mean		Direct	
	C.A.	Masked	C.A.	Masked	C.A.	Masked
IFC	1.697	2.202	1.517	1.864	-	-
MS-SSIM	0.793	0.837	0.712	0.745	-	-
PSNR	20.12	21.33	17.37	18.13	16.27	16.80
SSIM	0.717	0.775	0.540	0.587	0.549	0.596
VIF	0.200	0.284	0.244	0.302	-	-

IFC*	2.146	2.546	1.814	2.103	-	-
VIF*	1.036	1.254	0.730	0.845	-	-

* denotes the enhanced result as the reference.

3 Experiments

Several experimental details will be demonstrated in this section.

3.1 Mask evaluation

As shown in Figure 1(d) and Figure 1(e), we assessed two kinds of masks with the DRIVE benchmark data: (1) Direct generation, the mask without any fitting; (2) After fitting, the mask with ellipse-fitting and affine transformation. We investigated our masks by using 5 different similarity coefficients: Cosine Similarity, Dice Similarity, Jaccard Similarity, Pearson Correlation Similarity and Tanimoto Similarity. The statistics of results are listed in Table II.

3.2 Image evaluation

We assessed three scoring modes: "Y channel" (scoring by the Y channel), "Mean" (scoring by the average score of R, G and B channels) and "Direct" (scoring by the entire RGB image). In order to measure the generalization capability of our method, two types of objective quality evaluation methods were conducted: (1) the full-reference (FR) IQA algorithms; (2) the no-reference (NR) IQA models. By referring to [22], we deliberately selected several models from each type: (1) FR: PSNR, SSIM [23], MS-SSIM [24], IFC [25], and VIF [26]; (2) NR: NIQE [27], BLIINDS2 [28], BRISQE [29], BIQI [30], and ILNIQE [31]. As illustrated in Figure 6, when we used the aforesaid FR models to test our results, we aligned the original images with their results at first.

We will incline to analyze the NR results exhaustively, because there is no reference for us actually. As shown in Figure 7, we visualized each series of the hybrid test set by y-axis scatter plots. Besides, we also presented all of our selected NR models along the x-axis. And their global statistical information was summarized in Table III. From Table III, we could find that each statistical characteristic of NR models shows its individual style.

On the other hand, when we review our hybrid dataset again (which has been demonstrated completely in Table I), we can excavate something different from Figure 7. We determine that the test scores depend on their data sources. More concretely, BIQI works excellently in DRIVE, Kaggle, Od and Proc data series, in contrast to other series. But its scores in Vk series are not as good as others, especially for the results of "Y channel". Conversely, this situation does not appear in BLIINDS2.

Now, let us investigate the relationship between the FR modes and different scoring models. We can summarize something significant from Table IV. First, if we probe into both MS-SSIM and SSIM algorithms, their scores of "Y channel" are higher than those of "Mean". Another important aspect of analyzing this relationship is to detect the influence of two kinds of references. Basically, there are only few differences between the results of these two kinds of references, except IFC. It can be explained that there is no significant difference between two kinds of references as shown in Figure 6.

4 Conclusions

We have described a pipeline of fundus images enhancement. This new pipeline integrated many innovative modules, such as the FOV region extension module and the color restoration module. Relying on the test of a hybrid dataset, our method shows that it could improve recognition and reduce the influence of different environments. And it also gives us a chance to help mass screening of fundus diseases. Finally, our pipeline lets us see that we could establish a static method to handle diverse data sources.

References

[1] S. Chaudhuri, S. Chatterjee, N. Katz, M. Nelson, and M. Goldbaum, "Detection of blood vessels in retinal images using two-dimensional matched filters," IEEE Transactions on medical imaging, vol. 8, no. 3, pp. 263–269, 1989.

[2] R. Taylor, L. Lovelock, W. Tunbridge, K. Alberti, R. G. Brackenridge, P. Stephenson, and E. Young, "Comparison of non-mydriatic retinal photography with ophthalmoscopy in 2159 patients: mobile retinal camera study." Bmj, vol. 301, no. 6763, pp. 1243–1247, 1990.

[3] B. Shen and S. Mukai, "A portable, inexpensive, nonmydriatic fundus camera based on the raspberry pi R computer," Investigative Ophthalmology & Visual Science, vol. 57, no. 12, pp. 1657–1657, 2016.

[4] Diagnostic-imaging, "Portable Fundus Cameras – Volk Optical: Non-Mydriatic", Volk Optical. Accessed on: Jun. 11, 2018. [Online]. Available: https://www.volk.com/

[5] A. Bandara and P. Giragama, "A retinal image enhancement technique for blood vessel segmentation algorithm," in 2017 IEEE International Conference on Industrial and Information Systems (ICIIS). IEEE, 2017, pp. 1–5.

[6] E. Le Pennec and S. Mallat, "Image compression with geometrical wavelets," in Proceedings 2000 International Conference on Image Processing, vol. 1. IEEE, 2000, pp. 661–664.

[7] K. Zuiderveld, "Contrast limited adaptive histogram equalization," in Graphics gems IV. Academic Press Professional, Inc., 1994, pp. 474–485.

[8] G. Fang, N. Yang, H. Lu, and K. Li, "Automatic segmentation of hard exudates in fundus images based on boosted soft segmentation," in 2010 International Conference on Intelligent Control and Information Processing. IEEE, 2010, pp. 633–638.

[9] V. Zeljkovic, M. Bojic, C. Tameze, and V. Valev, "Classification algorithm of retina images of diabetic patients based on exudates detection," in 2012 International Conference on High Performance Computing & Simulation (HPCS). IEEE, 2012, pp. 167–173.

[10] K. Jin, M. Zhou, S.Wang, L. Lou, Y. Xu, J. Ye, and D. Qian, "Computer-aided diagnosis based on enhancement of degraded fundus photographs," Acta ophthalmologica,

vol. 96, no. 3, pp. e320–e326, 2018.
[11] D. J. Jobson, Z.-u. Rahman, and G. A. Woodell, "Properties and performance of a center/surround retinex," IEEE transactions on image processing, vol. 6, no. 3, pp. 451–462, 1997.
[12] Z.-u. Rahman, D. J. Jobson, and G. A.Woodell, "Multi-scale retinex for color image enhancement," in Proceedings of 3rd IEEE International Conference on Image Processing, vol. 3. IEEE, 1996, pp. 1003–1006.
[13] A. F. M. Hani, T. A. Soomro, H. Nugroho, and H. A. Nugroho, "Enhancement of colour fundus image and ffa image using retica," in 2012 IEEE-EMBS Conference on Biomedical Engineering and Sciences. IEEE, 2012, pp. 831–836.
[14] J. Staal, M. D. Abr`amoff, M. Niemeijer, M. A. Viergever, and B. Van Ginneken, "Ridge-based vessel segmentation in color images of the retina," IEEE transactions on medical imaging, vol. 23, no. 4, pp. 501–509, 2004.
[15] Featured Prediction Competition, "Diabetic Retinopathy Detection: Identify signs of diabetic retinopathy in eye images", Kaggle, Feb. 18, 2015. Accessed on: Jun. 11, 2018. [Online]. Available: https://www.kaggle.com/c/diabetic-retinopathy-detection/data
[16] A. R. Bhavsar, N. H. Atebara, and J. H. Drouilhet, "Diabetic Retinopathy," Medscape, Sep. 02, 2021 (Latest Updated). Accessed on: Jun. 11, 2018. [Online]. Available: https://emedicine.medscape.com/article/1225122-overview#showall
[17] A. Green and L. Green, "Ophthalmoscopy by red free light," American Journal of Ophthalmology, vol. 6, no. 1, pp. 16–18, 1923.
[18] H. Cohen, Complex analysis with applications in science and engineering, 2nd ed. Springer Science & Business Media, 2007.
[19] R. Betti, "Circle inversion and tessellations of the non-Euclidean plane," Lettera Matematica, vol. 6, no. 3, pp. 167–178, 2018.
[20] R. Urbina and A. Iglesias, "Circle inversion of twodimensional objects with mathematica," in International Conference on Computational Science and Its Applications. Springer, 2005, pp. 547–555.
[21] J. W. Gibbs, "Fourier's series," Nature, vol. 59, no. 1539, p.606, 1899.
[22] K. Ma, Q. Wu, Z. Wang, Z. Duanmu, H. Yong, H. Li, and L. Zhang, "Group mad competition-a new methodology to compare objective image quality models," in Proceedings of the IEEE Conference on Computer Vision and Pattern Recognition, 2016, pp. 1664–1673.
[23] Z. Wang, A. C. Bovik, H. R. Sheikh, E. P. Simoncelli et al., "Image quality assessment: from error visibility to structural similarity," IEEE transactions on image processing, vol. 13, no. 4, pp. 600–612, 2004. 7
[24] Z. Wang, E. P. Simoncelli, and A. C. Bovik, "Multiscale structural similarity for image quality assessment," in The Thrity-Seventh Asilomar Conference on Signals, Systems & Computers, 2003, vol. 2. Ieee, 2003, pp. 1398–1402.
[25] H. R. Sheikh, A. C. Bovik, and G. De Veciana, "An information fidelity criterion for image quality assessment using natural scene statistics," IEEE Transactions on image processing, vol. 14, no. 12, pp. 2117–2128, 2005.
[26] H. R. Sheikh and A. C. Bovik, "Image information and visual quality," IEEE Transactions on image processing, vol. 15, no. 2, pp. 430–444, 2006.
[27] A. Mittal, R. Soundararajan, and A. C. Bovik, "Making a "completely blind" image quality analyzer," IEEE Signal Processing Letters, vol. 20, no. 3, pp. 209–212, 2012.
[28] M. A. Saad, A. C. Bovik, and C. Charrier, "Blind image quality assessment: A natural scene statistics approach in the dct domain," IEEE transactions on Image Processing, vol. 21, no. 8, pp. 3339–3352, 2012.
[29] A. Mittal, A. K. Moorthy, and A. C. Bovik, "No-reference image quality assessment in the spatial domain," IEEE Transactions on image processing, vol. 21, no. 12, pp. 4695–4708, 2012.
[30] A. K. Moorthy and A. C. Bovik, "A two-step framework for constructing blind image quality indices," IEEE Signal processing letters, vol. 17, no. 5, pp. 513–516, 2010.
[31] L. Zhang, L. Zhang, and A. C. Bovik, "A feature-enriched completely blind image quality evaluator," IEEE Transactions on Image Processing, vol. 24, no. 8, pp. 2579–2591, 2015.